ACS Catalysis

Research Article

Cite This: ACS Catal. 2018, 8, 11615−11621

pubs.acs.org/acscatalysis

# Unveiling Charge-Separation Dynamics in CdS/Metal−Organic Framework Composites for Enhanced Photocatalysis

Hai-Qun Xu,[†,§] Sizhuo Yang,[‡,§] Xing Ma,[†,§] Jier Huang,*[,‡] and Hai-Long Jiang*[,†]

[†]Hefei National Laboratory for Physical Sciences at the Microscale, CAS Key Laboratory of Soft Matter Chemistry, Collaborative Innovation Center of Suzhou Nano Science and Technology, Department of Chemistry, University of Science and Technology of China, Hefei, Anhui 230026, P.R. China

[‡]Department of Chemistry, Marquette University, Milwaukee, Wisconsin 53201, United States

Supporting Information

**ABSTRACT:** Photocatalytic water splitting for $H_2$ production becomes one of the most favorable pathways for solar energy utilization, while the charge-separation dynamics in composite photocatalysts is largely elusive. In the present work, CdS-decorated metal−organic framework (MOF) composites, namely, CdS/UiO-66, have been synthesized and exhibit high $H_2$ production activity from photocatalytic water splitting, far surpassing the MOF and CdS counterparts, under visible light irradiation. Transient absorption (TA) spectroscopy has been adopted in this report to unveil the charge-separation dynamics in CdS/UiO-66 composites, a key process that dictates their function in photocatalysis. We show that, in addition to the preferable formation of fine CdS particles assisted by the MOF, effective electron transfer, which occurs from excited CdS to UiO-66, significantly inhibits the recombination of photogenerated charge carriers, ultimately boosting the photocatalytic activity for $H_2$ generation. This report on charge-separation dynamics for CdS−MOF composites affords significant insights for future fabrication of advanced composite photocatalysts.

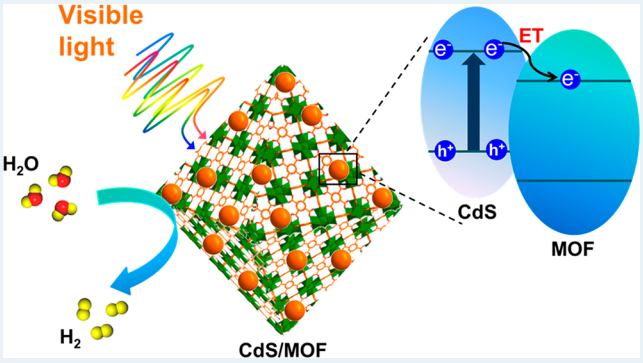


**KEYWORDS:** *metal−organic framework, cadmium sulfide, photocatalysis, hydrogen production, charge-separation dynamics*

## 1. INTRODUCTION

Photocatalytic $H_2$ production through water splitting represents a preferable approach to meet the future challenges of energy and environmental issues.[1] Significant research progress has been achieved with regards to the development of artificial photocatalytic systems based on semiconductors that can effectively perform light-driven $H_2$ generation reaction during the past several decades.[2−7] Among various semiconductors that have been employed, cadmium sulfide (i.e., CdS) is very much preferred due to its good visible light absorption ability and suited conduction band position that is sufficient to drive $H_2$ generation reaction.[8−12] Unfortunately, the photocorrosion-induced toxicity of $Cd^{2+}$, the inherent instability of CdS in non strongly alkaline conditions, the fast recombination of photoinduced electron−hole (e-h) pairs, and the limited surface catalytic sites restrict the application of pure CdS particles. Despite many attempts have been done to improve the catalytic activity of CdS, including modulating the CdS morphology[9] and the formation of composites with other materials, such as porous materials,[8] noble metals,[10] and semiconductors,[11] the development of efficient CdS-based photocatalysts is still a significant challenge.

Metal−organic frameworks (MOFs), emerging as a class of crystalline porous materials, have aroused broad interest in the past ∼20 years and proved to possess potential applications in a variety of fields,[13−16] including photocatalysis.[17−35] Compared with traditional semiconductor photocatalysts, MOFs feature porous structures with large surface area, and their structures and functionalities are readily tunable. Unfortunately, most MOFs show poor light response in the visible region, largely limiting their application in solar energy utilization.[25−35] Therefore, the fabrication of MOF-based composites with broadband spectral response would be highly desired to boost their photocatalysis under solar/visible irradiation.

With a view toward developing photocatalysts with high stability and efficiency, we have selected a representative stable MOF, UiO-66 with intrinsic photocatalytic $H_2$ production activity,[36−39] and fabricated CdS-decorated UiO-66 composites, hereafter named CdS/UiO-66 (Scheme 1), for photocatalytic $H_2$ generation. This system takes advantage of the merits of both CdS and the MOF while avoiding the drawbacks of each component. The CdS has the capability to harvest visible light, and UiO-66 carries high surface area

Received: August 14, 2018
Revised: October 29, 2018
Published: October 30, 2018






DOI: 10.1021/acscatal.8b03233
ACS Catal. 2018, 8, 11615−11621

**Scheme 1. Synthetic Process for CdS/UiO-66 Composites**

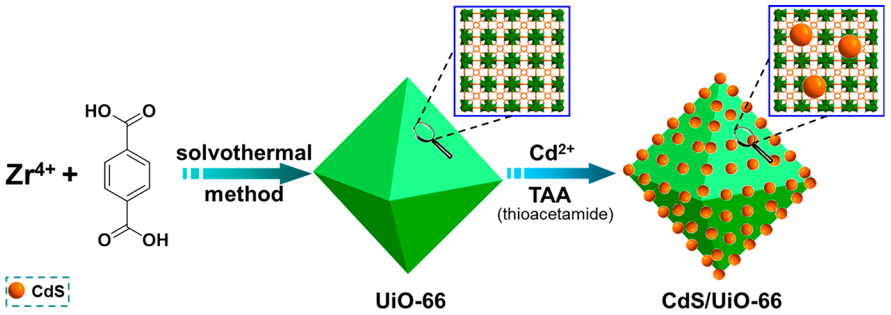


that can facilitate the dispersion of CdS on the MOF surface, thus providing more adsorption sites and photocatalytic reaction centers. Resorting to transient absorption (TA) spectroscopy, effective electron transfer (ET) from excited CdS to the MOF has been proved to greatly promote the charge separation in CdS and enhance the photocatalytic $H_2$ production activity of the CdS/UiO-66 composites. While enhanced photocatalysis over CdS/MOF and $TiO_2$/MOF composites was previously reported,[40−43] the charge-separation dynamics in CdS/MOF composites, which have been observed for the first time by TA spectroscopy, indicate the generation of long-lifetime electrons that give rise to much enhanced photocatalytic $H_2$ production activity.

## 2. EXPERIMENTAL SECTION

**2.1. Material and Instrumentation.** All chemicals were obtained from commercial sources and used directly unless particularly mentioned. Scanning electron microscopy (SEM) images were acquired on a field-emission scanning electron microanalyzer (Zeiss Supra 40 scanning electron microscope at an acceleration voltage of 5 kV). Transmission electron microscopy (TEM) and high-resolution transmission electron microscope (HRTEM) observations were conducted with a field-emission transmission electron microscope (JEOL JEM-2100F). Powder X-ray diffraction (XRD) patterns were collected on a Japan Rigaku MiniFlex 600 equipped with graphite-monochromated Cu K$\alpha$ radiation ($\lambda$ = 1.54178 Å). The ESCALAB 250 high-performance electron spectrometer using monochromatized Al K$\alpha$ ($h\nu$ = 1486.7 eV) as the excitation source was employed to produce the X-ray photoelectron spectroscopy (XPS) data. The $N_2$ sorption measurements were conducted with a Micromeritics ASAP 2020 instrument at 77 K. The Shimadzu UV-2700 spectrophotometer recorded the UV−vis diffuse reflectance spectra, using a white standard of $BaSO_4$ as a reference. The contents of CdS in CdS/UiO-66 composites were quantified by an Optima 7300 DV inductively coupled plasma atomic emission spectrometer (ICP-AES).

**2.2. Preparation of Samples.** The UiO-66 crystals were synthesized using $ZrCl_4$ and terephthalic acid ($H_2BDC$) as reactants according to the reported method.[30] The CdS nanoparticles (NPs) were in situ deposited onto the surface of UiO-66 crystals with $Cd(CH_3COO)_2{\cdot}2H_2O$ and thioacetamide (TAA) as cadmium and sulfur sources, respectively, at 10, 20, and 40 wt % CdS loadings, to give CdS/UiO-66(X) composites, where X denotes the CdS theoretical content (Scheme 1).

*2.2.1. Synthesis of UiO-66.* We referred to the previous report to prepare the UiO-66 with minor modifications.[30] Typically, 5 mL of dimethylformamide (DMF) solution of $ZrCl_4$ (18.64 mg) and 5 mL of DMF solution of $H_2BDC$ (13.28 mg) were mixed in a 20 mL glass vial. Following that, 1.2 mL of acetic acid was added, then sealed, and allowed to react at 120 °C for 24 h without stirring. The product was isolated by centrifugation and rinsed with DMF and MeOH. Finally, UiO-66 was dried at 60 °C under vacuum overnight.

*2.2.2. Synthesis of CdS/UiO-66(10).* Typically, 8.1 mg of $Cd(CH_3COO)_2{\cdot}2H_2O$ was dissolved in 10 mL of ethanol. Then, 40 mg of UiO-66 was mixed with the solution and then sonicated for 30 min. After that, the suspension was heated at 80 °C for 10 min, to which 10 mL of aqueous solution of thioacetamide (TAA, 2.3 mg) was injected into the flask dropwise with intense agitation and heating at 80 °C for another 30 min. Then, the suspension was heated at 80 °C for 30 min. The precipitates were filtered and rinsed with $H_2O$ and ethanol several times. Finally, the product was dried at 60 °C under vacuum for 12 h.

*2.2.3. Synthesis of CdS/UiO-66(20).* The synthetic procedure is almost the same as the synthesis of CdS/UiO-66(10), except for using 16.8 mg of $Cd(CH_3COO)_2{\cdot}2H_2O$ and 4.7 mg of TAA.

*2.2.4. Synthesis of CdS/UiO-66(40).* The synthetic procedure is almost the same as the synthesis of CdS/UiO-66(10), except for using 49.1 mg of $Cd(CH_3COO)_2{\cdot}2H_2O$ and 13.9 mg of TAA.

*2.2.5. Synthesis of CdS.* Typically, 92 mg of $Cd(CH_3COO)_2{\cdot}2H_2O$ was dissolved in 10 mL of ethanol. After that, the suspension was heated at 80 °C for 10 min, to which 10 mL of aqueous solution of TAA (26 mg) was injected into the flask dropwise with intense agitation and heating at 80 °C for another 30 min. Then, the suspension was heated at 80 °C for 30 min. The precipitates were filtered and rinsed with $H_2O$ and ethanol several times. Finally, the product was dried at 60 °C under vacuum for 12 h.

**2.3. Catalyst Characterization.** *2.3.1. Electrochemical Characterization.* The working electrodes were prepared by applying 15 $\mu$L of slurry to the surface of indium−tin oxide (ITO) glass plates and covering ~1 $cm^2$. The slurry was prepared by mixing 0.02 g of sample and 2 mL of ethanol. Electrochemical measurements were carried out with a Zahner Zennium electrochemical workstation by a conventional three-electrode cell, containing a graphite rod (counter electrode) and Ag/AgCl electrode (reference electrode). The experiments were completed at room temperature in 0.2 M $Na_2SO_4$ electrolyte deoxygenated in an $N_2$ stream.

*2.3.2. Photocatalytic Reaction.* A certain amount of the CdS/UiO-66(X) (with a fixed CdS amount of 2 mg) or 2 mg of CdS or 2 mg of UiO-66 was dispersed in 27 mL of acetonitrile and 1 mL of deionized water with 3 mL of lactic



DOI: 10.1021/acscatal.8b03233
ACS Catal. 2018, 8, 11615−11621

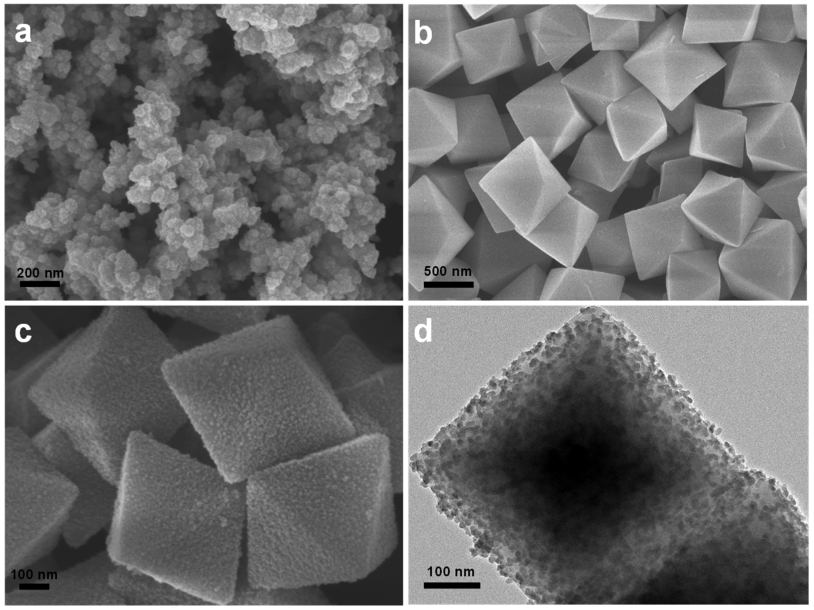


**Figure 1.** SEM images of (a) CdS and (b) UiO-66. (c) SEM and (d) TEM images of CdS/UiO-66(10).

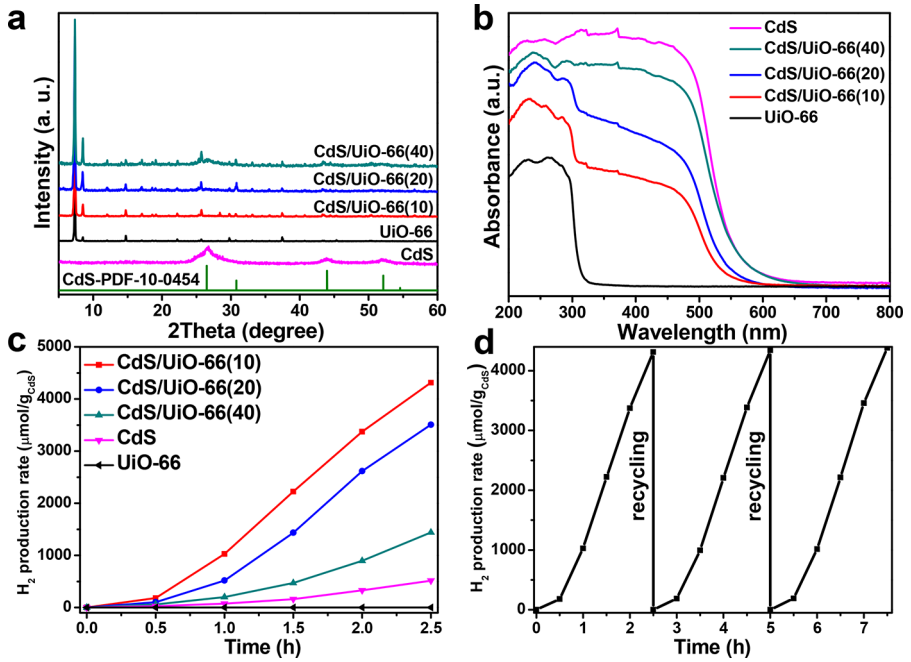


**Figure 2.** (a) Powder XRD profiles, (b) UV−vis diffuse reflectance spectra, and (c) photocatalytic $H_2$ production rates for CdS, UiO-66, and CdS/UiO-66 composites with altered weight ratios of CdS. (d) Recycling performance of CdS/UiO-66(10).

acid (being sacrificial reagent). Then the suspension was stirred in a 160 mL homemade reaction vessel and purged with $N_2$ for ∼60 min to exhaust air, followed by the 300 W Xe light irradiation with a UV cutoff filter ($\lambda$ > 380 nm). The reactions were further investigated by different amounts of CdS and CdS/UiO-66(X) (with CdS amount ranging from 5 to 100 mg, for testing photonic yield), which were dispersed in 4 mL of acetonitrile with 0.3 mL of deionized water and 1 mL of lactic acid. The suspension was stirred in a 160 mL homemade reaction vessel and purged with $N_2$ for ∼30 min to exhaust air, followed by the 300 W Xe light irradiation with a monochromatic light filter ($\lambda$ = 420 nm). Gas chromatography (Shimadzu GC-2014, argon as a carrier gas) using a thermal conductivity detector (TCD) was employed to measure the $H_2$ evolution during the reaction.

*2.3.3. Ultrafast Spectroscopy Characterizations.* The femtosecond transient absorption (TA) spectroscopy was collected through a regenerative amplified Ti-Sapphire laser system (Solstice, 800 nm, <100 fs FWHM, 3.5 mJ/pulse, 1 kHz repetition rate). Seventy-five percent of the 800 nm fundamental pulse was introduced into TOPAS to generate tunable pump wavelength. Twenty-five percent of the fundamental pulse was used to generate visible probe (450−750 nm) using a sapphire window. Helios ultrafast spectrometer (Ultrafast Systems, LLC) was employed to record the TA spectra. To make thin films for TA



DOI: 10.1021/acscatal.8b03233
ACS Catal. 2018, 8, 11615−11621

measurements, 1 mg of sample was added into 0.5 mL of Nafion (5% w/w in water and 1-propanol) in a glass vial. The hybrid was stirred for 2 h and then distributed uniformly on a piranha-etched glass. The samples were dried in air. The film samples were constantly translated in case of heating and permanent degradation. The pump power at 400 nm is 0.2 mW for all measurements.

## 3. RESULTS AND DISCUSSION

The actual mass fraction of CdS in the composites is close to the theoretical one, based on the ICP-AES analysis (Table S1). In the absence of MOF, CdS NPs easily aggregate together (Figure 1a and Figure S1). The UiO-66 microcrystals present a well-defined octahedral profile with smooth surface (Figure 1b). The SEM and TEM observations of CdS/UiO-66(10) indicate that the MOF is of great importance in the formation of small CdS NPs, which present a good dispersion on the external surface of UiO-66 octahedral crystals (Figure 1c and d). Along with a higher content of CdS introduced, it can be observed that more CdS NPs were decorated onto the MOF (Figure S2), in which 10 wt % loading of CdS/UiO-66(10) gives an excellent CdS dispersion. It is noteworthy that, once the CdS content increases up to 40 wt %, the CdS NPs are severely aggregated. As shown in the HRTEM image (Figure S3), the measured lattice fringes are assignable to the (111) face of cubic CdS. The close contact between CdS and UiO-66 would be favorable to the formation of heterojunctions between them and facilitate their charge transfer and separation.

The crystallinity of the CdS/UiO-66 was analyzed and confirmed by powder XRD (Figure 2a). The pure CdS obtained as a control in the absence of UiO-66 presents cubic phase structure (PDF No. 10-0454). The UiO-66 structure is retained after the decoration with CdS, and the characteristic powder XRD (PXRD) patterns of CdS are more intense with its higher loadings (Figure S4), in agreement with the CdS aggregation indicated by the SEM and TEM observation. XPS tests were applied to investigate the involved composition and interface feature of the CdS/UiO-66 composites (Figure S5). The XPS survey spectrum for CdS/UiO-66(10) shows the presence of Cd, S, Zr, O, and C, and no impurity peak can be observed (Figure S5a). For the high-resolution Cd 3d spectrum, the Cd $3d_{5/2}$ and Cd $3d_{3/2}$ peaks appear at around 405.0 and 411.8 eV, respectively, revealing the +2 oxidation state of the Cd element (Figure S5c).[44] In the high-resolution XPS spectrum of S 2p, the S $2p_{3/2}$ and S $2p_{1/2}$ peaks are located at 161.3 and 162.5 eV, respectively, suggesting the presence of $S^{2-}$ (Figure S5d).[45] These XPS results adequately support the existence of CdS in the CdS/UiO-66(10) hybrid. Compared with the binding energies of Cd 3d and S 2p in pure CdS, they present a negative shift in CdS/UiO-66 composite (Figure S5c and d). Meanwhile, there is a slight upshift in the binding energy of Zr 3d for CdS/UiO-66 composite in reference to that for pure UiO-66 (Figure S5b). These results indicate the interaction between CdS and UiO-66, instead of simple physical contact. The Brunauer−Emmett−Teller (BET) surface area of the composites increases with increasing content of UiO-66, which is ascribed to the high surface area of UiO-66 and nonporous structure of CdS (Figure S6). The UiO-66 has no absorption in the visible region, while CdS shows strong visible light absorption. After modifying UiO-66 with CdS, the UV−vis diffuse reflectance spectra of CdS/UiO-66 composites show absorption features of both components, and the absorption at the visible region becomes stronger with more CdS contained in the composites (Figure 2b), which further supports the presence of CdS in the composites. The color change of all samples from white to orange with increasing percentage of CdS has been recorded (Figure S7).

We then proceed to investigate the visible-light photocatalytic $H_2$ production performance of CdS/UiO-66 composites by water splitting. The experiments were carried out under the illumination of a Xe light equipped with a long-pass filter ($\lambda$ > 380 nm), and the reaction temperature was controlled by condensed water. Figure 2c shows the time profile of $H_2$ generation of CdS/UiO-66 composites with different contents of CdS. As expected, the system with UiO-66 alone does not generate $H_2$ because of its nonresponsive nature to visible light. The system with CdS only produces a small amount of $H_2$, suggesting that CdS has intrinsic photocatalytic activity. However, in the presence of both CdS and UiO-66, i.e., CdS/UiO-66 composites, the amount of $H_2$ produced is significantly enhanced, suggesting the important role UiO-66 plays in the photocatalytic reaction. Interestingly, the photocatalytic activity of CdS/UiO-66 composites decreases along with the increase of CdS content, where the CdS/UiO-66(10) shows the best $H_2$ production activity (1725 $\mu$mol $g_{CdS}^{-1}$ $h^{-1}$). This $H_2$ production rate is ~8.4 times higher than that of CdS. Moreover, the photocatalytic activity of CdS/UiO-66(10) is higher than most of reported CdS-based composites with other porous materials (Table S2). This can be ascribed to the improved dispersion of CdS NPs in CdS/UiO-66 composites with lower content of CdS, preventing CdS particle aggregation and thus exposing more reaction sites. The stability of these systems was evaluated by recycling experiments. The catalytic activity of CdS/UiO-66(10) does not decrease within three cycles of experiment, suggesting its stability and recyclability. This is further supported by powder XRD profile and SEM/TEM images, demonstrating that the structure, morphology, and crystallinity of CdS/UiO-66(10) have negligible change before and after catalysis (Figures S8−S10).

Given that the photocatalytic rate is not proportional to the surface area of the photocatalyst and, accordingly, not to the mass of the photocatalyst,[46] we have further investigated the photonic yields of CdS and CdS/UiO-66(X) with different surface areas. The dependence of $H_2$ production rate on CdS amount, accompanied with different catalyst amounts, has been examined (Figure 3).[47] With a small percentage of CdS, CdS/UiO-66(10) exhibits an initially high $H_2$ production rate

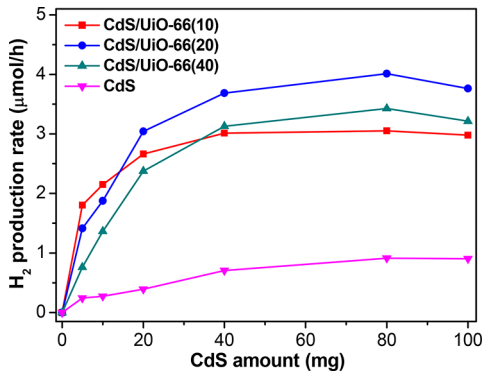


**Figure 3.** Dependence of photocatalytic $H_2$ production activity/rate on the CdS amount, accompanied with different catalyst amounts.



DOI: 10.1021/acscatal.8b03233
ACS Catal. 2018, 8, 11615−11621

due to the preferable formation of fine CdS nanoparticles and heterojunction between CdS and UiO-66. As the amount of the CdS catalyst gradually increases, more CdS/UiO-66(10) is accordingly required to maintain the same CdS amount. In this case, the relatively large amount of the catalyst in the reaction system would weaken penetration depth and increase scattering of the incident light, which would weaken the excitation of CdS in CdS/UiO-66(10) in reference to CdS/UiO-66(20) and CdS/UiO-66(40). As a result, in the plateau regions, the optimal rate of CdS/UiO-66(20) is the highest among all CdS/UiO-66(X), manifesting that CdS/UiO-66(20) provides the highest photonic yield under the experimental conditions.[46] Moreover, the apparent quantum efficiency (AQE) of CdS and CdS/UiO-66 composites with different weight percentages of CdS for photocatalytic $H_2$ production are also evaluated (based on the data of Figure 3). The results show that CdS/UiO-66(20) achieves the highest AQE of ~0.85% under irradiation at 420 nm (Table S3). The optimal rates and AQE of all CdS/UiO-66(X) are much higher than those of CdS, further verifying the importance of constructing CdS/UiO-66 composite photocatalyst.

To gain information on the photocatalytic mechanism and the specific roles CdS and UiO-66 played in catalysis, we investigated charge-separation dynamics in CdS/UiO-66 composites through femtosecond transient absorption (fs-TA) spectroscopy.[48−50] Figure 4 presents the fs-TA spectra of

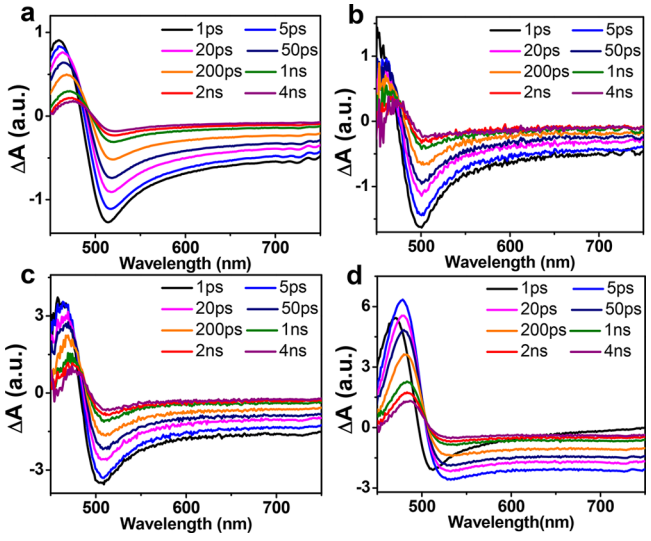


**Figure 4.** Transient femtosecond absorption spectra of (a) CdS, (b) CdS/UiO-66(10), (c) CdS/UiO-66(20), and (d) CdS/UiO-66(40) under 400 nm excitation.

CdS/UiO-66 in different ratios following 400 nm excitation. Two features were observed in the spectra of CdS (Figure 4a), containing a negative feature centered around 500 nm and a positive absorption band from 450 to 480 nm. The former can be attributed to the 1S exciton bleach band in CdS because of the state filling of 1S(e) level at the conduction band.[48] The positive absorption band centered at ~460 nm is able to be ascribed to the stark-effect-induced absorption resulting from the presence of 1S exciton.[51] Besides these two features, a broad bleach band at >600 nm was also observed in the TA spectra of CdS. This spectral feature, consistent with previous literature data,[49] can be assigned to the stimulated emission of CdS. The amplitude of these spectral features was quenched in the presence of methyl viologen ($MV^{2+}$) (Figure S11), suggesting that they are associated with electron signals, consistent with the assignment above. The TA spectra of CdS/UiO-66 having different CdS contents show similar spectral features as that of CdS (Figure 4b−d). However, the kinetics of 1S exciton bleach recovery, which reflects the electron lifetime in the conduction band, is enhanced in the presence of UiO-66, suggesting the enhanced depopulation of conduction band electrons in the composites. The depopulation of 1S electrons can arise from electron transfer or energy transfer from CdS to UiO-66. Energy transfer can be excluded in this system due to negligible overlap of CdS emission band with the absorption spectrum of UiO-66 (negligible absorption in visible light scope).

To elucidate the feasibility of electron transfer between CdS and UiO-66 under visible light irradiation, Mott−Schottky plots were recorded at different frequencies (Figures S12 and S14). The lowest unoccupied molecular orbital (LUMO) of UiO-66 is located at −0.6 V vs normal hydrogen electrode (NHE) (Figure S12). Given the UiO-66 bandgap measured to be 4.1 eV based on the Tauc plot (Figure S13), its highest occupied molecular orbital (HOMO) can be estimated as 3.5 V vs NHE. The conduction band (CB) of CdS is determined to be −0.7 V vs NHE (Figure S14). The suited band positions of UiO-66 and CdS make it thermodynamically possible for photogenerated electron transfer in CdS/UiO-66 composites. As a result, we believe that enhanced exciton bleach recovery in CdS/UiO-66 composites with respect to that in CdS sample is due to electron transfer process from CdS to UiO-66. Interestingly, the exciton bleach recovery is faster in CdS/UiO-66 composites with a lower amount of CdS (Figure 5a), i.e.,

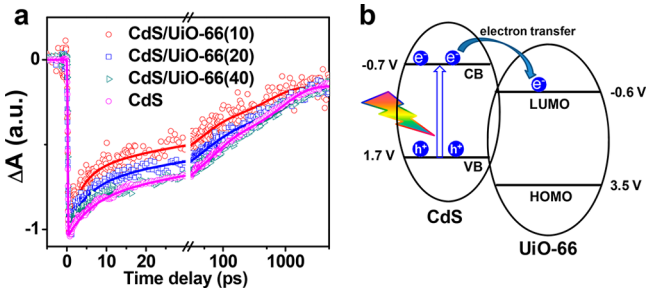


**Figure 5.** (a) Comparison of kinetic traces at 650 nm among CdS and CdS/UiO-66 composites with altered CdS contents. (b) Energetic scheme that illustrates electron transfer dynamics from CdS to UiO-66.

electron transfer rate increases in the following order: CdS ≈ CdS/UiO-66(40) < CdS/UiO-66(20) < CdS/UiO-66(10). These results, following the same trend as their photocatalytic performance, imply that faster electron transfer process from CdS to UiO-66 in CdS/UiO-66 composites with a lower amount of CdS facilitates charge separation in the composites, ultimately enhancing $H_2$ generation efficiency (Figure 5b). These results together manifest that UiO-66 not only gives a significant influence to improve the dispersion of CdS on its surface but also act as charge-separation material/cocatalyst, facilitating charge separation and boosting $H_2$ generation.

## 4. CONCLUSION

In summary, well-dispersed CdS was stabilized on the surface of a MOF support, UiO-66, to provide CdS/UiO-66



DOI: 10.1021/acscatal.8b03233
ACS Catal. 2018, 8, 11615−11621

composites, which exhibit remarkably higher activity than that of each component toward photocatalytic $H_2$ production. The MOF support greatly improves the dispersion and downsizes CdS particles, which enable the exposure of more adsorption and reactive sites. Moreover, for the first time, it is unambiguously evidenced that electron transfer occurs from excited CdS to MOF by means of transient absorption spectroscopy, resulting in a charge-separated state with electrons located at UiO-66 and holes at the valence band of CdS, which slows down the charge-recombination process and, ultimately, boosts the efficiency of photocatalytic $H_2$ production. This work enables a deeper understanding of electron transfer in semiconductor−MOF composites. Given the synergetic enhancements in photocatalytic activity often found in composite materials, our findings highlight the benefits of constructing such architectures and should stimulate further research in the development of advanced composite materials for efficient photocatalysis.

## ■ ASSOCIATED CONTENT

### Supporting Information

The Supporting Information is available free of charge on the ACS Publications website at DOI: 10.1021/acscatal.8b03233.

Full experimental details, TEM and SEM images, PXRD patterns, XPS, $N_2$ sorption isotherms, photos, TA spectra, Mott−Schottky plots, Tauc plot, ICP, and AQE of CdS and CdS/UiO-66 (PDF)

## ■ AUTHOR INFORMATION


### Corresponding Authors

*E-mail: jier.huang@marquette.edu.cn.
*E-mail: jianglab@ustc.edu.cn.

### ORCID

Jier Huang: 0000-0002-2885-5786
Hai-Long Jiang: 0000-0002-2975-7977


### Author Contributions

§H.-Q.X., S.Y., and X.M. contributed equally to this work.

### Notes

The authors declare no competing financial interest.

## ■ ACKNOWLEDGMENTS

This work was supported by the NSFC (21725101, 21673213, and 21521001) and the National Research Fund for Fundamental Key Project (2014CB931803). J.H. and S.Y. acknowledge the support from National Science Foundation (DMR-1654140).

## ■ REFERENCES


(1) Lewis, N. S.; Nocera, D. G. Powering the Planet: Chemical Challenges in Solar Energy Utilization. *Proc. Natl. Acad. Sci. U. S. A.* **2006**, *103*, 15729−15735.

(2) Zou, Z.; Ye, J.; Sayama, K.; Arakawa, H. Direct Splitting of Water under Visible Light Irradiation with an Oxide Semiconductor Photocatalyst. *Nature* **2001**, *414*, 625−627.

(3) Wang, X.; Maeda, K.; Thomas, A.; Takanabe, K.; Xin, G.; Carlsson, J. M.; Domen, K.; Antonietti, M. A Metal-Free Polymeric Photocatalyst for Hydrogen Production from Water under Visible Light. *Nat. Mater.* **2009**, *8*, 76−80.

(4) Kudo, A.; Miseki, Y. Heterogeneous Photocatalyst Materials for Water Splitting. *Chem. Soc. Rev.* **2009**, *38*, 253−278.

(5) Chen, X.; Shen, S.; Guo, L.; Mao, S. S. Semiconductor-Based Photocatalytic Hydrogen Generation. *Chem. Rev.* **2010**, *110*, 6503−6570.

(6) Christoforidis, K. C.; Syrgiannis, Z.; La PArola, V.; Montini, T.; Petit, C.; Stathatos, E.; Godin, R.; Durrant, J. R.; Prato, M.; Fornasiero, P. Metal-Free Dual-Phase Full Organic Carbon Nanotubes/g-$C_3N_4$ Heteroarchitectures for Photocatalytic Hydrogen Production. *Nano Energy* **2018**, *50*, 468−478.

(7) Liu, J.; Liu, Y.; Liu, N.; Han, Y.; Zhang, X.; Huang, H.; Lifshitz, Y.; Lee, S.-T.; Zhong, J.; Kang, Z. Metal-Free Efficient Photocatalyst for Stable Visible Water Splitting via a Two-Electron Pathway. *Science* **2015**, *347*, 970−974.

(8) Peng, R.; Wu, C.-M.; Baltrusaitis, J.; Dimitrijevic, N. M.; Rajh, T.; Koodali, R. T. Ultra-Stable CdS Incorporated Ti-MCM-48 Mesoporous Materials for Efficient Photocatalytic Decomposition of Water under Visible Light Illumination. *Chem. Commun.* **2013**, *49*, 3221−3223.

(9) Yu, J.; Yu, Y.; Zhou, P.; Xiao, W.; Cheng, B. Morphology-Dependent Photocatalytic $H_2$-Production Activity of CdS. *Appl. Catal., B* **2014**, *156−157*, 184−191.

(10) Wu, K.; Chen, Z.; Lv, H.; Zhu, H.; Hill, C. L.; Lian, T. Hole Removal Rate Limits Photodriven $H_2$ Generation Efficiency in CdS-Pt and CdSe/CdS-Pt Semiconductor Nanorod-Metal Tip Heterostructures. *J. Am. Chem. Soc.* **2014**, *136*, 7708−7716.

(11) Zhang, L. J.; Li, S.; Liu, B. K.; Wang, D. J.; Xie, T. F. Highly Efficient CdS/$WO_3$ Photocatalysts: Z-scheme Photocatalytic Mechanism for Their Enhanced Photocatalytic $H_2$ Evolution under Visible Light. *ACS Catal.* **2014**, *4*, 3724−3729.

(12) Tang, Z.-R.; Han, B.; Han, C.; Xu, Y.-J. One Dimensional CdS Based Materials for Artificial Photoredox Reactions. *J. Mater. Chem. A* **2017**, *5*, 2387−2410.

(13) Cook, T. R.; Zheng, Y.-R.; Stang, P. J. Metal-Organic Frameworks and Self-Assembled Supramolecular Coordination Complexes: Comparing and Contrasting the Design, Synthesis, and Functionality of Metal-Organic Materials. *Chem. Rev.* **2013**, *113*, 734−777.

(14) Furukawa, H.; Cordova, K. E.; O'Keeffe, M.; Yaghi, O. M. The Chemistry and Applications of Metal-Organic Frameworks. *Science* **2013**, *341*, 1230444.

(15) Zhou, H.-C.; Kitagawa, S. Metal-Organic Frameworks (MOFs). *Chem. Soc. Rev.* **2014**, *43*, 5415−5418.

(16) Li, B.; Wen, H.-M.; Cui, Y.; Zhou, W.; Qian, G.; Chen, B. Emerging Multifunctional Metal-Organic Framework Materials. *Adv. Mater.* **2016**, *28*, 8819−8860.

(17) Wang, C.; Xie, Z.; deKrafft, K. E.; Lin, W. Doping Metal-Organic Frameworks for Water Oxidation, Carbon Dioxide Reduction, and Organic Photocatalysis. *J. Am. Chem. Soc.* **2011**, *133*, 13445−13454.

(18) Fu, Y.; Sun, D.; Chen, Y.; Huang, R.; Ding, Z.; Fu, X.; Li, Z. An Amine-Functionalized Titanium Metal-Organic Framework Photocatalyst with Visible-Light-Induced Activity for $CO_2$ Reduction. *Angew. Chem., Int. Ed.* **2012**, *51*, 3364−3367.

(19) Wang, S.; Yao, W.; Lin, J.; Ding, Z.; Wang, X. Cobalt Imidazolate Metal-Organic Frameworks Photosplit $CO_2$ under Mild Reaction Conditions. *Angew. Chem., Int. Ed.* **2014**, *53*, 1034−1038.

(20) Xu, H.-Q.; Hu, J.; Wang, D.; Li, Z.; Zhang, Q.; Luo, Y.; Yu, S.-H.; Jiang, H.-L. Visible-Light Photoreduction of $CO_2$ in a Metal-Organic Framework: Boosting Electron-Hole Separation via Electron Trap States. *J. Am. Chem. Soc.* **2015**, *137*, 13440−13443.

(21) Zhang, H.; Wei, J.; Dong, J.; Liu, G.; Shi, L.; An, P.; Zhao, G.; Kong, J.; Wang, X.; Meng, X.; Zhang, J.; Ye, J. Efficient Visible-Light-Driven Carbon Dioxide Reduction by a Single-Atom Implanted Metal-Organic Framework. *Angew. Chem., Int. Ed.* **2016**, *55*, 14310−14314.

(22) Dhakshinamoorthy, A.; Asiri, A. M.; García, H. Metal-Organic Framework (MOF) Compounds: Photocatalysts for Redox Reactions and Solar Fuel Production. *Angew. Chem., Int. Ed.* **2016**, *55*, 5414−5445.




DOI: 10.1021/acscatal.8b03233
*ACS Catal.* 2018, 8, 11615−11621

(23) Choi, K. M.; Kim, D.; Rungtaweevoranit, B.; Trickett, C. A.; Barmanbek, J. T. D.; Alshammari, A. S.; Yang, P.; Yaghi, O. M. Plasmon-Enhanced Photocatalytic $CO_2$ Conversion within Metal-Organic Frameworks under Visible Light. *J. Am. Chem. Soc.* **2017**, *139*, 356−362.
(24) Wang, Y.; Huang, N.-Y.; Shen, J.-Q.; Liao, P.-Q.; Chen, X.-M.; Zhang, J.-P. Hydroxide Ligands Cooperate with Catalytic Centers in Metal-Organic Frameworks for Efficient Photocatalytic $CO_2$ Reduction. *J. Am. Chem. Soc.* **2018**, *140*, 38−41.
(25) Kataoka, Y.; Sato, K.; Miyazaki, Y.; Masuda, K.; Tanaka, H.; Naito, S.; Mori, W. Photocatalytic Hydrogen Production from Water Using Porous Material $[Ru_2(p\text{-}BDC)_2]_n$. *Energy Environ. Sci.* **2009**, *2*, 397−400.
(26) Fateeva, A.; Chater, P. A.; Ireland, C. P.; Tahir, A. A.; Khimyak, Y. Z.; Wiper, P. V.; Darwent, J. R.; Rosseinsky, M. J. A Water-Stable Porphyrin-Based Metal-Organic Framework Active for Visible-Light Photocatalysis. *Angew. Chem., Int. Ed.* **2012**, *51*, 7440−7444.
(27) Zhou, T.; Du, Y.; Borgna, A.; Hong, J.; Wang, Y.; Han, J.; Zhang, W.; Xu, R. Post-Synthesis Modification of a Metal-Organic Framework to Construct a Bifunctional Photocatalyst for Hydrogen Production. *Energy Environ. Sci.* **2013**, *6*, 3229−3234.
(28) Pullen, S.; Fei, H.; Orthaber, A.; Cohen, S. M.; Ott, S. Enhanced Photochemical Hydrogen Production by a Molecular Diiron Catalyst Incorporated into a Metal-Organic Framework. *J. Am. Chem. Soc.* **2013**, *135*, 16997−17003.
(29) Saha, S.; Das, G.; Thote, J.; Banerjee, R. Photocatalytic Metal-Organic Framework from CdS Quantum Dot Incubated Luminescent Metallohydrogel. *J. Am. Chem. Soc.* **2014**, *136*, 14845−14851.
(30) Xiao, J.-D.; Shang, Q.; Xiong, Y.; Zhang, Q.; Luo, Y.; Yu, S.-H.; Jiang, H.-L. Boosting Photocatalytic Hydrogen Production of a Metal-Organic Framework Decorated with Platinum Nanoparticles: the Platinum Location Matters. *Angew. Chem., Int. Ed.* **2016**, *55*, 9389−9393.
(31) Dong, X.-Y.; Zhang, M.; Pei, R.-B.; Wang, Q.; Wei, D.-H.; Zang, S.-Q.; Fan, Y.-T.; Mak, T. C. W. A Crystalline Copper (II) Coordination Polymer for the Efficient Visible-Light-Driven Generation of Hydrogen. *Angew. Chem., Int. Ed.* **2016**, *55*, 2073−2077.
(32) Kim, D.; Whang, D. R.; Park, S. Y. Self-Healing of Molecular Catalyst and Photosensitizer on Metal-Organic Framework: Robust Molecular System for Photocatalytic $H_2$ Evolution from Water. *J. Am. Chem. Soc.* **2016**, *138*, 8698−8701.
(33) An, Y.; Liu, Y.; An, P.; Dong, J.; Xu, B.; Dai, Y.; Qin, X.; Zhang, X.; Whangbo, M.-H.; Huang, B. $Ni^{II}$ Coordination to Al-Based Metal-Organic Framework Made from 2-Aminoterephthalate for Photocatalytic Overall Water Splitting. *Angew. Chem., Int. Ed.* **2017**, *56*, 3036−3040.
(34) Yang, S.; Pattengale, B.; Kovrigin, E. L.; Huang, J. Photoactive Zeolitic Imidazolate Framework as Intrinsic Heterogeneous Catalysts for Light-Driven Hydrogen Generation. *ACS Energy Lett.* **2017**, *2*, 75−80.
(35) Xiao, J.-D.; Han, L.; Luo, J.; Yu, S.-H.; Jiang, H.-L. Integration of Plasmonic Effects and Schottky Junctions into Metal-Organic Framework Composites: Steering Charge Flow for Enhanced Visible-Light Photocatalysis. *Angew. Chem., Int. Ed.* **2018**, *57*, 1103−1107.
(36) Cavka, J. H.; Jakobsen, S.; Olsbye, U.; Guillou, N.; Lamberti, C.; Bordiga, S.; Lillerud, K. P. A New Zirconium Inorganic Building Brick Forming Metal Organic Frameworks with Exceptional Stability. *J. Am. Chem. Soc.* **2008**, *130*, 13850−13851.
(37) Gomes Silva, C.; Luz, I.; Llabrés i Xamena, F. X.; Corma, A.; García, H. Water Stable Zr−Benzenedicarboxylate Metal-Organic Frameworks as Photocatalysts for Hydrogen Generation. *Chem. - Eur. J.* **2010**, *16*, 11133−11138.
(38) He, J.; Wang, J.; Chen, Y.; Zhang, J.; Duan, D.; Wang, Y.; Yan, Z. A Dye-Sensitized Pt@UiO-66(Zr) Metal-Organic Framework for Visible-Light Photocatalytic Hydrogen Production. *Chem. Commun.* **2014**, *50*, 7063−7066.
(39) Yuan, Y.-P.; Yin, L.-S.; Cao, S.-W.; Xu, G.-S.; Li, C.-H.; Xue, C. Improving Photocatalytic Hydrogen Production of Metal-Organic Framework UiO-66 Octahedrons by Dye-Sensitization. *Appl. Catal., B* **2015**, *168−169*, 572−576.
(40) He, J.; Yan, Z.; Wang, J.; Xie, J.; Jiang, L.; Shi, Y.; Yuan, F.; Yu, F.; Sun, Y. Significantly Enhanced Photocatalytic Hydrogen Evolution under Visible Light over CdS Embedded on Metal-Organic Frameworks. *Chem. Commun.* **2013**, *49*, 6761−6763.
(41) Shen, L.; Liang, S.; Wu, W.; Liang, R.; Wu, L. CdS-Decorated UiO-66($NH_2$) Nanocomposites Fabricated by a Facile Photodeposition Process: an Efficient and Stable Visible-Light-Driven Photocatalyst for Selective Oxidation of Alcohols. *J. Mater. Chem. A* **2013**, *1*, 11473−11482.
(42) Jiang, Z.; Liu, J.; Gao, M.; Fan, X.; Zhang, L.; Zhang, J. Assembling Polyoxo-Titanium Clusters and CdS Nanoparticles to a Porous Matrix for Efficient and Tunable $H_2$-Evolution Activities with Visible Light. *Adv. Mater.* **2017**, *29*, 1603369.
(43) Crake, A.; Christoforidis, K. C.; Kafizas, A.; Zafeiratos, S.; Petit, C. $CO_2$ Capture and Photocatalytic Reduction Using Bifunctional $TiO_2$/MOF Nanocomposites under UV-vis Irradiation. *Appl. Catal., B* **2017**, *210*, 131−140.
(44) Ge, L.; Zuo, F.; Liu, J.; Ma, Q.; Wang, C.; Sun, D.; Bartels, L.; Feng, P. Synthesis and Efficient Visible Light Photocatalytic Hydrogen Evolution of Polymeric g-$C_3N_4$ Coupled with CdS Quantum Dots. *J. Phys. Chem. C* **2012**, *116*, 13708−13714.
(45) Huang, Y.; Chen, Y.; Hu, C.; Zhang, B.; Shen, T.; Chen, X.; Zhang, M. Q. 'Bridge' Effect of CdS Nanoparticles in the Interface of Graphene-Polyaniline Composites. *J. Mater. Chem.* **2012**, *22*, 10999−11002.
(46) Qureshi, M.; Takanabe, K. Insights on Measuring and Reporting Heterogeneous Photocatalysis: Efficiency Definitions and Setup Examples. *Chem. Mater.* **2017**, *29*, 158−167.
(47) Kisch, H.; Bahnemann, D. Best Practice in Photocatalysis: Comparing Rates or Apparent Quantum Yields. *J. Phys. Chem. Lett.* **2015**, *6*, 1907−1910.
(48) Wu, K.; Zhu, H.; Liu, Z.; Rodríguez-Córdoba, W.; Lian, T. Ultrafast Charge Separation and Long-Lived Charge Separated State in Photocatalytic CdS-Pt Nanorod Heterostructures. *J. Am. Chem. Soc.* **2012**, *134*, 10337−10340.
(49) Yin, X.-L.; He, G.-Y.; Sun, B.; Jiang, W.-J.; Xue, D.-J.; Xia, A.-D.; Wan, L.-J.; Hu, J.-S. Rational Design and Electron Transfer Kinetics of $MoS_2$/CdS Nanodots-on-Nanorods for Efficient Visible-Light-Driven Hydrogen Generation. *Nano Energy* **2016**, *28*, 319−329.
(50) Utterback, J. K.; Grennell, A. N.; Wilker, M. B.; Pearce, O. M.; Eaves, J. D.; Dukovic, G. Observation of Trapped-Hole Diffusion on the Surfaces of CdS Nanorods. *Nat. Chem.* **2016**, *8*, 1061−1066.
(51) Zhu, H.; Song, N.; Lian, T. Controlling Charge Separation and Recombination Rates in CdSe/ZnS Type I Core-Shell Quantum Dots by Shell Thicknesses. *J. Am. Chem. Soc.* **2010**, *132*, 15038−15045.


DOI: 10.1021/acscatal.8b03233
*ACS Catal.* 2018, 8, 11615−11621